Construction and Building Materials 281 (2021) 122606

Contents lists available at ScienceDirect

Construction and Building Materials

journal homepage: www.elsevier.com/locate/conbuildmat

The effect of graphite and slag on electrical and mechanical properties of electrically conductive cementitious composites

Junbo Sun [a], Sen Lin [b], Genbao Zhang [c,*], Yuantian Sun [d], Junfei Zhang [e], Changfu Chen [f], Amr M. Morsy [g,h], Xiangyu Wang [a]

[a] Australasian Joint Research Centre for Building Information Modelling, Curtin University, Perth 6102, Australia
[b] College of Mechanical and Vehicle Engineering, Hunan University, Changsha, Hunan 410082, China
[c] College of Civil Engineering, Hunan City University, Yiyang 413000, Hunan, China
[d] School of Mines, China University of Mining and Technology, Xuzhou 221116, China
[e] School of Civil, Environmental and Mining Engineering, The University of Western Australia, Crawley 6009, WA, Australia
[f] College of Civil Engineering, Hunan University, China
[g] School of Architecture, Building and Civil Engineering, Loughborough University, Leicestershire LE11 3TU, United Kingdom
[h] Department of Civil Engineering, Cairo University, Giza 12613, Egypt

HIGHLIGHTS

- A new program evaluating the impact of graphite and slag, and curing time.
- Optimized slag and graphite to achieve balanced electrical and mechanical properties.
- A microstructural interpretation to reveal distributions of conductive filler and C-S-H gel.

ARTICLE INFO

Article history:
Received 11 December 2020
Received in revised form 1 February 2021
Accepted 2 February 2021

Keywords:
Graphite
Slag
Compressive behavior
Flexural behavior
Conductive composite
Cementitious composite

ABSTRACT

Electrically conductive cementitious composites (ECCCs) have become a significant research interest in structural health monitoring. The use of graphite in ECCCs can significantly improve their electrical performance, however, with unsatisfactory friction resistance because of the graphite's smooth microsurfaces. Slag can be incorporated with graphites into ECCCs to achieve good performance in both of mechanical resistance and electrical conductivity. This study investigated the impact of graphite and slag on the electrical and mechanical behaviors of ECCCs. Two hundred and eighty ECCC specimens were prepared with two different types of slags and with various conductivity ingredient fractions and curing times. The specimens were tested for compressive strength, flexural strength, and electrical resistance. It was concluded the 4% graphite content in ECCCs can significantly enhance electrical conductivity with moderate decrease in compressive and flexural strengths. Slags were found to improve both electrical conductivity and mechanical properties of ECCCs. The best results could be obtained with optimized contents of steel slag, blast furnace slag, and graphite. Finally, the microstructural mechanisms of the ECCC specimens were analyzed using scanning electron microscope (SEM) for graphite and slag. Variable sensitivity analysis was performed to allow for optimization of ingredient contents.

1. Introduction

Cement-based materials have developed rapidly due to their superior mechanical performance including high loading resistance and excellent cost efficiency [1–3]. However, to ensure safety of cement-based structures under large service loading conditions over their service lifespans, structural health monitoring (SHM) technologies have been introduced [4–6]. On succession of piezoresistive effect, SHM methods were developed to measure stresses using acoustic emissions [7], digital imaging [8–10], and fiber sensors [11–13]. However, the proposed SHM methods negates indirect methodologies and may have negative effects on the physical and mechanical properties of cement-based structures [14,15]. Accordingly, electrically conductive cementitious

* Corresponding author.
E-mail addresses: senlin@hnu.edu.cn (S. Lin), gbzhang@hnu.edu.cn (G. Zhang), yuantiansun@cumt.edu.cn (Y. Sun), junfei.zhang@research.uwa.edu.au (J. Zhang), cfchen@hnu.edu.cn (C. Chen), a.morsy@lboro.ac.uk (A.M. Morsy), Xiangyu.Wang@curtin.edu.au (X. Wang).

https://doi.org/10.1016/j.conbuildmat.2021.122606
0950-0618/

composites (ECCCs) can be an ideal solution. As smart composite materials, ECCCs can themselves serve as sensors to monitor the structural electrical resistivity to evaluate their structural integrity [16]. Simultaneously, ECCCs avail multiple functions including mechanical resistance, thermal conductivity in large-scale bridges, snow melting of the roadbed, and electromagnetic shielding of microwave pollution [17–20].

Studies have shown that conductive concrete incorporated by functional fillers can change the electrical resistivity to various degrees ranging from 10^6 to 10^9 Ω·cm [21]. Han et al. [22] conducted a thorough review of conductive fillers that can effectively improve the electrical behavior and self-sensing features. Among these conductive fillers, carbon ingreddients such as carbon fiber (CF), carbon black (CB), graphite powder (GP) as well as corresponding formations demonstrated outstanding potential in cementitious composite due to their excellent electrical conductivities, light weights, and dielectric properties [23–25]. For instance, 2 vol% multi-layer graphene was found to result in a 15.6% change in electrical resistivity in composite structures [26]. Singh et al. [27] found a shielding effectiveness (SE) value towards microwave pollution of −46 dB for graphene oxide-ferro fluid composite (30 wt%). Chen et al. [28] explored graphene oxide–carbon fibre concrete to get a reflection loss value of −34 dB.

Moreover, with the fast developments in nanotechnology, the nanometer carbon materials attracted considerable attention among researchers comprising graphite nano-platelets (NGP), multi-walled carbon nanotubes (MWCNT), silicon carbide nanowires (SiCNW), carbon nanotubes (CNT) and carbon nanofibers (CNF) [29,30]. However, nano-size magnitude carbon fillers equip unstable crystal microstructures. This causes huge challenge when the materials are used at large dosage, high cost and smooth interface micro-surfaces, which have negative effects on the mechanical properties because of the physical microstructure, rheology, hydration speed, and mechanical behavior [31–33]. For practical application of ECCCs, it is critical to optimize ingredient contents to achieve the desired electrical and mechanical properties. Metal slags can be ideal as an auxiliary blending ingredient in carbon conductive fillers.

As prevailing industry by-products in engineering practice, metal slags such as copper slag (CS), steel slag (SS), and ground granulated blast-furnace slag (GGBS) exhibit high conductive characteristics and wear resistance, which make them excellent ingredient candidates for ECCCs [34–36]. Slags equip uniform particle distributions that can replace fine aggregates (FA) in cementitious composite, enhancing durability, toughness, compressive and flexural performance [37–39]. Some slags have proven suitable to equip potential hydraulic properties owing to their similar chemical composition to ordinary Portland cement [40,41]. Accordingly, the use of carbon material and slags ought to render balanced conductive performance, mechanical performance, cost-effectiveness and environmental-friendliness.

In this study, ECCC mixtures were developed using GP, SS, and GGBS powders. The effects of these ingredients on the mechanical properties (compressive and flexural strengths) and electrical properties (electrical conductivity) of ECCC mixtures were investigated at various curing ages. Scanning electron microscope (SEM) was used to analyze the microscale mechanisms that take place in the ECCC mixtures. Lastly, sensitivity analysis was conducted to allow for optimization of ingredient contents. Overall, this study provides a basis for studying the influence of different filler contents, age, temperature, and other factors on the electrical conductivity and basic mechanical properties of concrete, producing composite conductive concrete.

2. Experimental program

2.1. Cement composite design

The composite comprised of ordinary Portland cement (P.O 52.5 R) as a binder, fine silica sand (SS) ranging from 0.2 to 0.4 mm (fineness modulus of 2.6), and coarse gravel aggregate ranging from 5 to 10 mm. A polycarboxylate-based superplasticizer (SP) was used to reduce segregation intensity, yield stress and cement sensitivity [42,43]. As for the main conductive ingredient, graphite powder (GP) was chosen given its outstanding high carbon content (larger than 98%) and low electrical resistivity [44]. Additionally, steel slag (SS) particle, and ground granulated blast-furnace slag (GGBS) were deployed because of their cost-effectiveness and environmental-friendliness. X-ray fluorescence (XRF) tests were performed to measure the chemical composition of graphite and slags [45]. The properties of superplasticizer admixture is demonstrated in Table 1. The chemical compositions and physical specifications of the cement and conductive fillers are presented in Table 2. The scanning electron microscope (SEM) captured the micro-structural characteristics of ECCCs with conductive fillers, as shown in Fig. 1.

As presented in Table 2, graphite powder (GP) has more than 98% of carbon with high purity to demonstrate considerable conductive capacity. It owns giant covalent structure with free delocalized electrons around carbon atom. The electron exchanges or local displacements can thus transfer electric currents in the direction of the proposed electric field. Besides, the graphite has considerable glossy microstructures which can fill aggregate voids and micropores in cementitious materials rendering dense microstructures. Proper fraction of GP improves the mechanical strength within interfacial zones, and forms conductive networks in the Calcium–Silicate–Hydrate (C–S–H) gel [46]. However, excessive graphite can result in agglomeration effect that reduces mixture consistency, which can negatively affect the mechanical behavior. The smooth, glossy microstructures of graphite (Fig. 1a) may reduce the internal friction in the mixture, and in turn the mechanical strength [47]. As a result, the dosage of graphite is crucial in ECCCs to achieve the desired electrical and mechanical behaviors.

As presented in Table 2, ground granulated blast-furnace slag GGBS has mainly CaO and SiO_2 which contribute to more than 67% of its chemical composition. The particle size ranges from 23 to 37 μm and the density reaches 2840 kg/m^3. The material exhibits crystal structures from the SEM photo (Fig. 1b). The sharp edges improve the bonding strength between the C–S–H gel and the aggregate, which enhances the durability and mechanical resistance of the mixture.

As presented in Table 2, steel slag (SS) contains higher ferrite fraction and density (3670 kg/m^3) compared to GGBS. The particle size ranges from 50 to 75 μm. The microstructure SEM photo shows that the steel slag has crystal structures because of the crushing treatment (Fig. 1c). Massive sharp-edged square crystals 0.5 to 1 μm in size could be observed on the slag microsurfaces. This microstructure enhances the bond with cement, which in turn enhances the mechanical behaviour of the mixture. The effect of

Table 1
Properties of superplasticizer admixture.

PH	Density (g/ml)	Water-Reducing rate (%)	Air Content (%)	Chlorinity (%)
7–8	1.1	37%	2	0.02

the SS rough microstructure on the mechanical behavior of ECCCs can compensate the negative effect of the GP smooth microstructure.

In this study, GP was incorporated into the binder material at three different percentages (2%, 4%, and 6%) by weight of the binder material, to explore the effect of GP on the ECCC electrical conductivity. In addition, three cement replacement ratios by slag (20%, 30%, and 40%), referred to as TW group, TH group, and FO group. In each group, three SS mass ratios of (25%, 50%, and 75%) were adopted to validate the optimized slag distribution. For comparison purposes, one additional ordinary concrete sample without conductive fillers was prepared as a control sample. Table 3 presents the mass proportion of ingredients for per cubic meter mixture of ECCC composite. A total of 280 ECCC specimens were prepared for three types of experiments, i.e. 112 specimens for testing electrical conductivity, 84 specimens for testing compressive strength, and 84 specimens for testing flexural strength.

Table 2
Chemical compositions and physical details of cement and conductive fillers.

Ordinary Portland Cement		**Ground Granulated Blast-Furnace Slag (GGBS)**	
Chemical Compositions		**Chemical Compositions**	
CaO	63.40%	CaO	37.14%
SiO_2	20.10%	SiO_2	31.0%
Al_2O_3	4.60%	Al_2O_3	15.60%
Fe_2O_3	2.80%	MgO	8.51%
SO_3	2.70%	SO_3	2.40%
MgO	1.30%	Fe_2O_3	1.80%
Na_2O	0.60%	MnO	0.10%
Total chloride	0.02%		
Physical Properties		**Physical Properties**	
Density	3.20 kg/m^3	Specific gravity	2.84
Fineness index	390 m^2/kg	Specific surface area	472 m^2/kg
Normal consistency	27%	Relative strength	100%
Setting time initial	120 min	Pozzolanic Activity at 7 days	78%
Setting time final	210 min	Ignition loss 0.6%	
Loss on ignition	3.80%	Particle size distribution	23–37.4 μm
Steel Slag (SS)		**Graphite Powder (GP)**	
Chemical Compositions		**Chemical Compositions**	
CaO	31.49%	Carbon	98.5%
SiO_2	14.6%	Ash Content	0.90%
MgO	13.8%		
Al_2O_3	5.71%		
SO_3	2.40%		
Fe_2O_3	21.3%		
Physical Properties		**Physical Properties**	
Specific gravity	3.67	Specific gravity	0.33
Relative strength	100%	Melting Point	4200 ℃
Temperature rise	18.8 ℃	Moisture Content	0.35%
Particle size distribution	50–75 μm	Particle size distribution	10–37.4 μm

2.2. Graphite powder dispersion and cement mixture fabrication

An ultrasonic processor was used for GP dispersion experiment by the ultrasonic vibration. The intelligent vibrator generates 400 W intensity through an amplitude transformer with a frequency range of 20 to 25 kHz and a working temperature of 0 to 40 ℃. The instrument processes up to 70% powder ratio of its capacity, which is equivalent to 100 mL powder. Later, the amplitude transformer with a diameter of ¼“ was soaked at ¼” of probe length in material solution. Simultaneously, a silane coupling agent was added as a bridge to cohesively bond conductive fillers, which improves conductive network distribution uniformity. A dispersing agent was used to facilitate dispersion and render a uniform conductive network [48].

The preparation steps of ECCC sample using ultrasonic processor was shown in Fig. 2. Before dispersion treatment, the GP is soaked in an acetone solution for 1 h to promote surface activation and is later dried at 60℃ for 12 h. This is because original GP obtains impurity upon surface, which negates the microstructural friction behaviour and thus reduces mechanical strength. The acetone solution is utilized as activator. Besides, the GP particles are fine and lightweight, that could lead to aggregation effects, i.e. the ingredient demonstrates poor consistency. Thereby, the activated GP with a dispersing agent (10 wt% of GP) and a coupling agent (5 wt% of GP) were poured into a water solution (80 mL). The ultrasonic device vibrated the solution for 480 s to activate the dispersion effect and coupling film. During this process, the

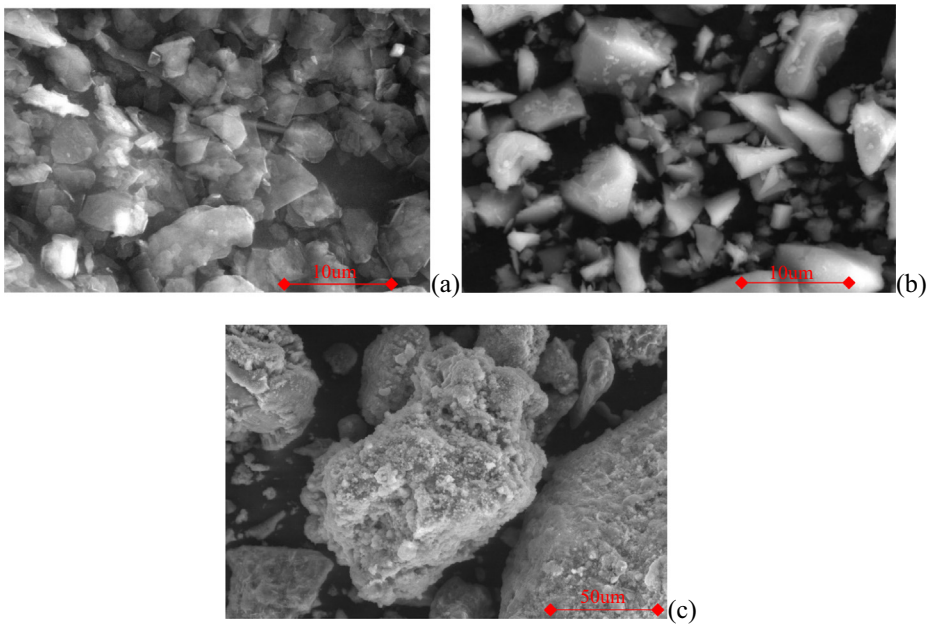

Fig. 1. Microscale structure of (a) GP; (b) GGBS; and (c) SS.

Table 3
Ingredient mass proportion of ECCC composite (per cubic meter mixture).

ID	OPC (kg)	Gravel (kg)	Sand (kg)	Water (kg)	SP (kg)	GP (kg)	GP Mass Ratio	Slag Substitution Ratio	SS (kg)	GGBS(kg)
Control	450	1302.6	884.6	125	1.42	0	0	0	0	0
TW252	360	1302.6	884.6	125	1.42	9	2%	20%	22.5	67.5
TW254	360	1302.6	884.6	125	1.42	18	4%	20%	22.5	67.5
TW256	360	1302.6	884.6	125	1.42	27	6%	20%	22.5	67.5
TW502	360	1302.6	884.6	125	1.42	9	2%	20%	45	45
TW504	360	1302.6	884.6	125	1.42	18	4%	20%	45	45
TW506	360	1302.6	884.6	125	1.42	27	6%	20%	45	45
TW752	360	1302.6	884.6	125	1.42	9	2%	20%	67.5	22.5
TW754	360	1302.6	884.6	125	1.42	18	4%	20%	67.5	22.5
TW756	360	1302.6	884.6	125	1.42	27	6%	20%	67.5	22.5
TH252	315	1302.6	884.6	125	1.42	9	2%	30%	45	90
TH254	315	1302.6	884.6	125	1.42	18	4%	30%	45	90
TH256	315	1302.6	884.6	125	1.42	27	6%	30%	45	90
TH502	315	1302.6	884.6	125	1.42	9	2%	30%	67.5	67.5
TH504	315	1302.6	884.6	125	1.42	18	4%	30%	67.5	67.5
TH506	315	1302.6	884.6	125	1.42	27	6%	30%	67.5	67.5
TH752	315	1302.6	884.6	125	1.42	9	2%	30%	90	45
TH754	315	1302.6	884.6	125	1.42	18	4%	30%	90	45
TH756	315	1302.6	884.6	125	1.42	27	6%	30%	90	45
FO252	270	1302.6	884.6	125	1.42	9	2%	40%	67.5	112.5
FO254	270	1302.6	884.6	125	1.42	18	4%	40%	67.5	112.5
FO256	270	1302.6	884.6	125	1.42	27	6%	40%	67.5	112.5
FO502	270	1302.6	884.6	125	1.42	9	2%	40%	90	90
FO504	270	1302.6	884.6	125	1.42	18	4%	40%	90	90
FO506	270	1302.6	884.6	125	1.42	27	6%	40%	90	90
FO752	270	1302.6	884.6	125	1.42	9	2%	40%	112.5	67.5
FO754	270	1302.6	884.6	125	1.42	18	4%	40%	112.5	67.5
FO756	270	1302.6	884.6	125	1.42	27	6%	40%	112.5	67.5

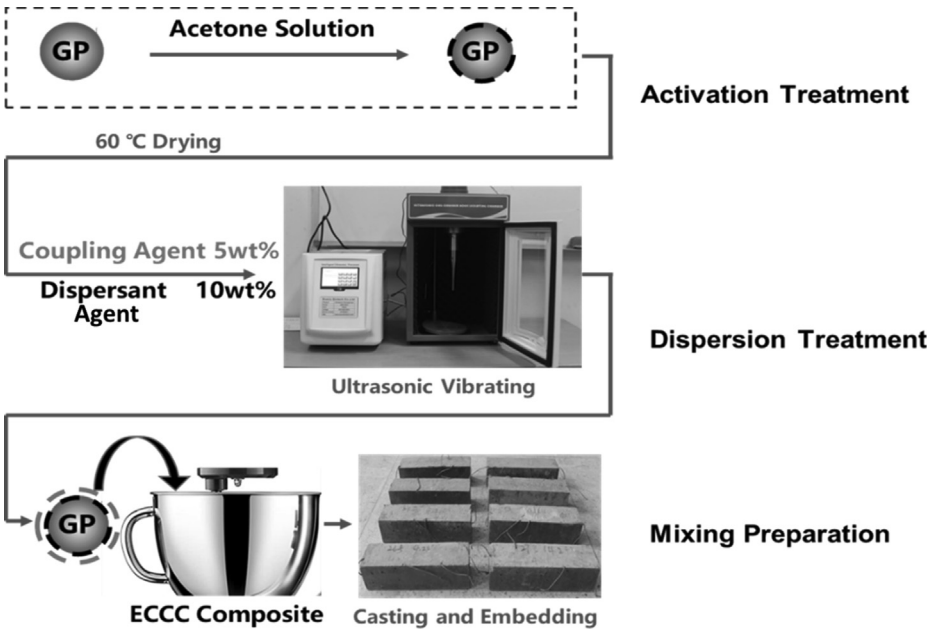

Fig. 2. ECCC sample preparation steps.

solution was vibrated for 2 s and then paused for 5 s to minimize liquid overheating. The solution was cooled down to around 21 ± 2 ℃ and was finally added into the dry mixture components according to the following specimen preparation procedure.

Dry mixture ingredients including cement, gravel, sand underwent mixing treatment for 5 min in a container. The SS and GGBS were then scattered into the container for 30 s to facilitate uniform distribution. Meanwhile, the proposed solution composite is then blended with the superplasticizer (SP) and was later separated into two equal portions. After stirring for 300 s, the dry composite was blended with one solution portion, followed by an 80 s mixing. The second solution portion was then sprinkled over the composite with over 200 s as stirring continued to produce the ECCC composite. After 30-second vibration to decrease trapped bubbles, the composite was finally cast according to AS1141.51 1996 [49]. All samples were stored in a moist cabinet for 28 days, according to their experiment date, with an ambient curing temperature of 20 ± 1 °C and a curing relative humidity of 95 ± 5%.

2.3. Electrical conductivity experiment

The experiment used four-pole method to test the 28-day electrical resistivity of the ECCC samples as depicted in Fig. 3. The samples were cast into 100 × 100 × 400 mm, and metal-mesh-electrodes with a size of 100 mm × 100 mm were parallelly embedded in the sample with a 120 mm interval in an equidistant manner. A digital multimeter was utilized to record the ECCC electrical resistivity through copper wires connected to metal meshes [50,51]. The electrical resistivity was calculated using Eq. (1), as follows:

$$\rho = 100 * \frac{UA}{IL} \tag{1}$$

where ρ denotes electrical resistivity (Ω·cm); U denotes voltage (V); I denotes electric current (A); A denotes cross-sectional area of concrete specimen (m^2); and L denotes distance between electrodes (m).

2.4. Mechanical performance experiments

Compressive and flexural strength tests were conducted on the ECCC samples to determine the influence of the conductive fillers on their mechanical performance at different curing ages in compliance with the AS1012.14 (1991) [52] and AS1012.9 (2014) [53]. After curing at 7, 14 and 28 days respectively, samples of the 28 design configurations measuring 50 × 50 × 50 mm were proposed in compressive experiments, and samples measuring 50 × 50 × 200 mm were manufactured for the flexural experiments. Three samples were prepared for every design configuration and for every test type. That is, the total number of samples prepared for mechanical experiments was 168 (84 samples for compressive strength tests and 84 samples for flexural strength tests). A digital servo-hydraulic universal testing machine (2000 kN capacity) was set to provide a loading rate of 0.5 MPa/s for the compression experiment and 0.03 MPa/s for the flexural experiment until ultimate strengths have been reached. Note that the 3-point flexural strength tests were ultilized with the loading points at 140 mm spacing. All loading displacement curves were automatically obtained until failure. The flexural strength was calculated using Eq. (2), as follows:

$$f_t = \frac{FL_f}{b_t h^2} \tag{2}$$

where f_t denotes flexural strength (MPa); F denotes fracture load (N); L_f denotes span length (mm); h denotes cross-section depth (mm); and b_t denotes cross-section width (mm).

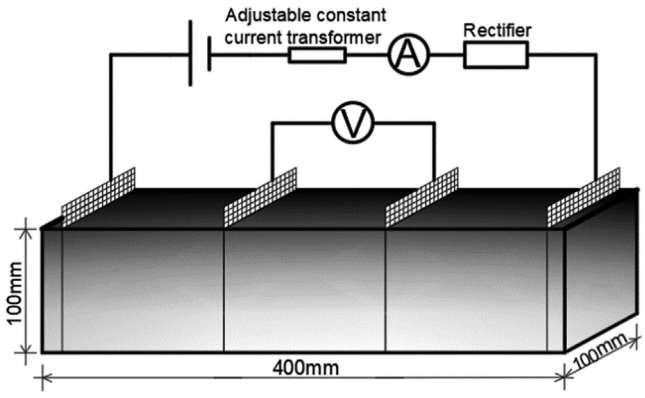

Fig. 3. Schematic diagram of four-electrode method.

3. Results and discussions

The results of the electrical conductance and mechanical strength (compression and flexural) tests are presented in Table 4. The results are discussed in detail in the following subsections.

3.1. Mechanical performance

Overall, compared to the ordinary concrete control sample (49.5 MPa compressive strength and 3.9 MPa flexural strength), the incorporation of GP negatively affected the mechanical behavior as observed in the results of samples tested at different curing ages (hydration periods). Samples with GP content of 6% exhibited significant lower strength compared to control sample. For instance, the compressive strength of sample FO256 was found to be 52% that of the control sample. The addition of GP to the ECCC mixture lubricates the microstructures that reduce the interface friction of the composite [54–56]. Simultaneously, slag substitution (20% of cement) enhances compressive strength (e.g., 7.8% increase for TW752 sample compared to control sample). This increase compensates the adverse effect of GP on the mechanical performance of ECCCs. The mechanical improvement observed by introduced the slag could be attributed to their crystal structures, which enhance the bond between the aggregates and the C–S–H gel [57,58]. However, a threshold for the maximum practical effect slag has on the mechanical performance of the mixture was found to correspond to slag replacement ratio of 30%. At this threshold, cement binder is insufficient to fill the gaps between rough aggregates, and thus weakens the compressive strength [59–61]. Compared to GGBS, SS provided better improvement to the mechanical performance of ECCCs.

The compressive strengths of the ECCC samples prepared according to the 27 mixture designs adopted in this study are shown in Fig. 4. For TW group samples (20% slag replacement) with SS ratios of 25% of the total slag content, the compressive strength decreased with increasing GP content (2, 4, and 6%), where the measured values were 46.4, 43.3, and 36.3 MPa, respectively. Similarly, samples with SS ratios of 50 and 75% of the total slag content exhibited compressive strength decrease with increasing GP content. It was noticed that the increase of GP content from 2 to 4% did not reduce the compressive strength (-1.2% on average) of the ECCC as much as it did when increased from 4 to 6% (-15.7% on average). It was also observed that the compressive strength of ECCCs increases with increasing the SS to total slag ratio at various curing ages.

Similar trends were observed for flexural strength as shown in Fig. 5. The flexural strength decreases with increasing GP content. This observation was consistent among samples prepared with the same slag contents. Considering the SS to total slag ratio, a higher value gives rise to flexural strength to the applied load in all hydration periods. Similar to compressive strength results, it was noticed that the increase of GP content from 2 to 4% did not reduce the flexural strength of the ECCC as much as it did when increased from 4 to 6%. It was also observed that the flexural strength of ECCCs increases with increasing the SS to total slag ratio at various curing ages.

3.2. Electrical conductivity

As shown in Fig. 6, the electrical resistivity reduced with increased slag content. For instance, the resistivity of the TW group samples (20% slag replacement and 6% GP content) decreased from 6.8 × 10^5 to 5.5 × 10^5 to 3.5 × 10^5 Ω.cm upon increasing the SS ratio of the total slag content from 25 to 30 to 40%, respectively. On the other hand, the electrical resistivity increased with increas-

Table 4
Mechanical performance and conductive resistance for ECCC composites.

ID	Slag Ratio	SS Ratio of Total Slag	GP Ratio	Electrical Conductivity (Ω·cm)				Compressive Strength (MPa)			Flexural Strength (MPa)		
				7 days	14 days	21 days	28 days	7 days	14 days	28 days	7 days	14 days	28 days
Control	0	0	0	1,933,751	2,315,122	2,572,178	4,205,411	38.1	44.6	49.5	3	3.5	3.9
TW252	20%	25%	2%	234,286	274,254	420,050	684,174	35.8	42	46.4	2.9	3.4	3.8
TW254		25%	4%	81,619	109,676	107,935	211,397	32.5	37	43.3	2.7	3.1	3.6
TW256		25%	6%	50,239	73,206	92,344	999,878	25.5	31	36.3	2	2.5	2.9
TW502		50%	2%	304,972	447,514	533,701	601,659	38.1	45.7	50.8	3	3.6	4
TW504		50%	4%	76,807	81,325	159,036	151,125	35	43.5	49.1	2.7	3.3	3.8
TW506		50%	6%	40,000	40,941	79,058	81,032	26.5	36	42.3	2.3	2.8	3
TW752		75%	2%	252,703	320,656	530,898	550,322	38.5	49	53.4	2.9	3.7	4.1
TW754		75%	4%	54,720	78,731	97,715	111,227	37.4	48.3	52.8	2.8	34	4
TW756		75%	6%	33,333	54,902	58,169	62,788	28.5	36.9	45	2.6	3	3.2
TH252	30%	25%	2%	277,754	459,143	547,005	530,416	24.5	31.3	34.7	2.3	3	3.3
TH254		25%	4%	26,605	45,183	49,541	49,978	22.5	30	33.8	2.2	2.9	3.1
TH256		25%	6%	8409	19,710	20,152	25,199	17.7	23.3	29.8	1.8	2.2	2.9
TH502		50%	2%	121,673	177,947	250,950	401,248	28.5	32.5	40.5	2.4	3.1	3.55
TH504		50%	4%	6701	11,082	15,893	24,985	26.9	29.7	37.9	2.3	2.95	3.45
TH506		50%	6%	4963	5948	6277	9559	18.1	25.8	35.2	2.1	2.6	3
TH752		75%	2%	157,895	196,382	191,447	310,131	30.3	38.8	43.2	2.5	3.2	3.7
TH754		75%	4%	4482	6436	6413	9599	27	33.3	40	2.4	3	3.51
TH756		75%	6%	1362	1911.2	1888	3025	19.9	27.7	36.9	2.3	2.8	3.15
FO252	40%	25%	2%	175,683	207,338	255,612	330,127	18.5	27.9	34	1.8	2.8	3.3
FO254		25%	4%	10,454	12,924	16,945	22,055	17.2	24.2	30.5	1.7	2.4	3.1
FO256		25%	6%	929	1230	1705	1995	11.3	16.2	23.7	1.5	2.2	2.4
FO502		50%	2%	90,252	123,187	167,528	228,359	26.5	34.6	40.2	2.15	2.7	3.5
FO504		50%	4%	1767	2912	5101	5050	20.5	29.1	36.9	2	2.6	3.2
FO506		50%	6%	393	476	738	820	11.4	16.9	27.2	1.9	2.3	2.7
FO752		75%	2%	34,317	46,051	55,596	81,085	24.1	33.2	42.1	2.3	2.8	3.6
FO754		75%	4%	332	505	674	1054	23.3	33.2	41.5	2.1	2.75	3.5
FO756		75%	6%	88	123	202	250	12.6	17.3	29.3	2	2.5	3

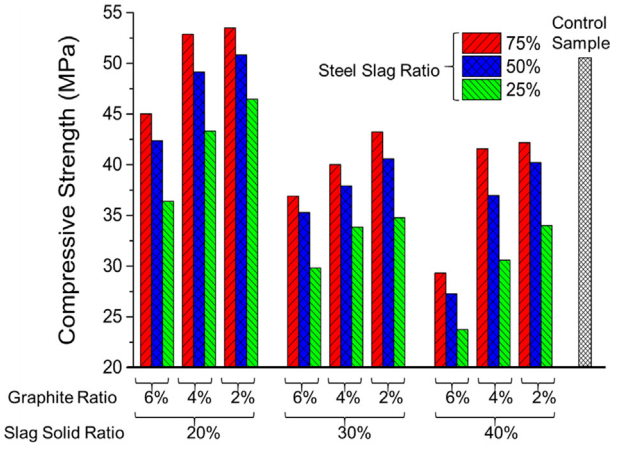

Fig. 4. Compression strength of ECCC samples.

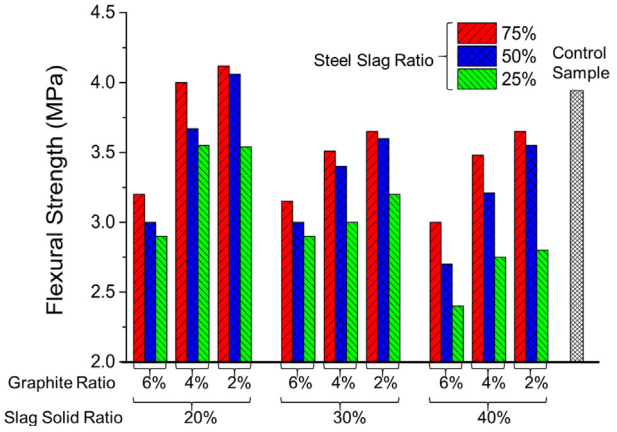

Fig. 5. Flexural strength of ECCC samples.

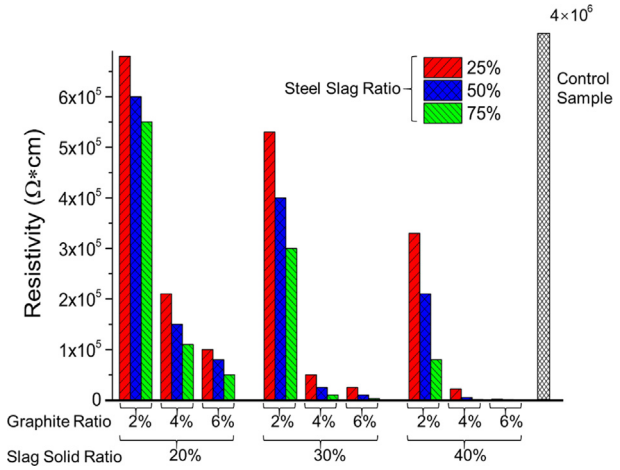

Fig. 6. Electerical resistivity of ECCC samples.

ing the GP content. This trend was observed among samples prepared at the same slag contents. It was also observed that the electrical resistivity decreased with increasing the SS ratio. It was noticed that among the samples prepared with a slag content of 40%, the resistivity was close to zero when the GP content was smaller than 4% despite the increase in SS ratio. This indicates that the resistivity depends on the different factors variably.

In conclusion, the design mixtures of ECCCs should be optimized to achieve balanced mechanical and electrical properties, such as the design of sample FO754 that included 25% SS, 15% GGBS, and 4% GP. This design rendered compressive strength of 41.5 MPa, flexural strength of 3.5 MPa, and electrical resistivity of 1054 Ω·cm, reaching a balanced state among other design mixture counterparts.

3.3. Microstructure analysis

Typical microstructural photos for ECCC samples with SS, SP, and GGBS fillers were presented in Fig. 7. Fig. 7a shows the microstructure of the ECCC sample with the optimum design (sample FO754) that exhibited balanced mechanical and electrical properties. As can be seen in the Fig., the GP and SS are uniformly distributed and the C–S–H gel fills well within the aggregate skeleton, which indicates that uniform distribution of conductive fillers can improve the conductivity of ECCCs. The filled gaps between the C–S–H gel improves the bonding effect between the aggregates and cementitious matrix. In contrast, Fig. 7b depicts the microstructure of the ECCC sample with the poorest mechanical and electrical properties (sample FO256). The conductive fillers and the C–S–H gel appear concentrated at localized zones (poorly distributed) within the mixture.

A schematic diagram of the conductive concrete mechanism is shown in Fig. 8. When GP is distributed uniformly, the conductivity of the concrete increases. Additional slag can produce silica (SiO_2) in the conductive concrete and boost its mechanical strength [70]. The C–S–H gel also plays an important role in improving both the mechanical and electrical performance as it fills up the micropores of the mixture and develops tighter bonds [62,63]. Besides, SS, which contains ferrite, can promote the conductivity of ECCCs.

3.4. Variable sensitivity analysis

As described earlier, different variables (SS ratio, GP ratio, and GGBS ratio) affect the mechanical and electrical performance of ECCCs. In this study, a sensitivity analysis was performed to obtain the specific importance of each variable using standard regression coefficient (C_i) presented in Eq. (3), as follows:

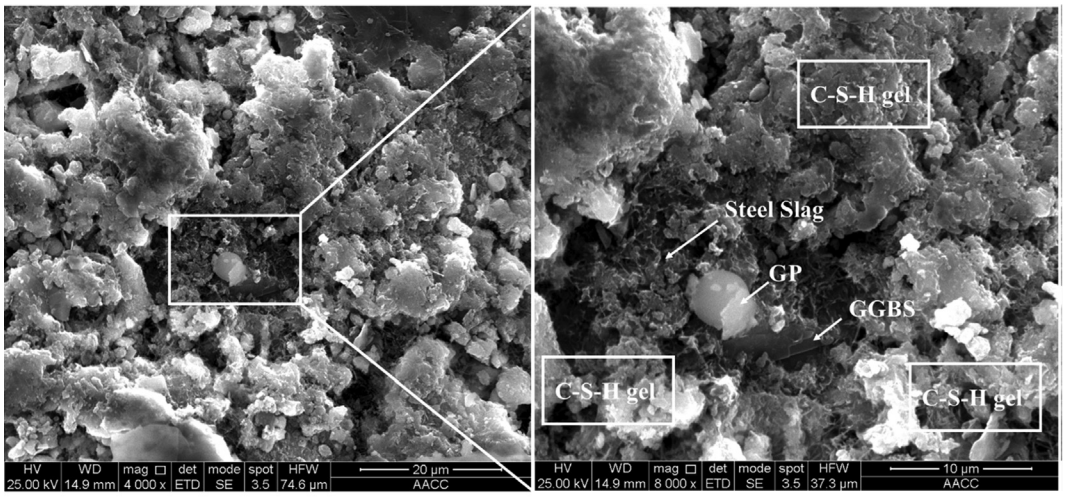

(a)

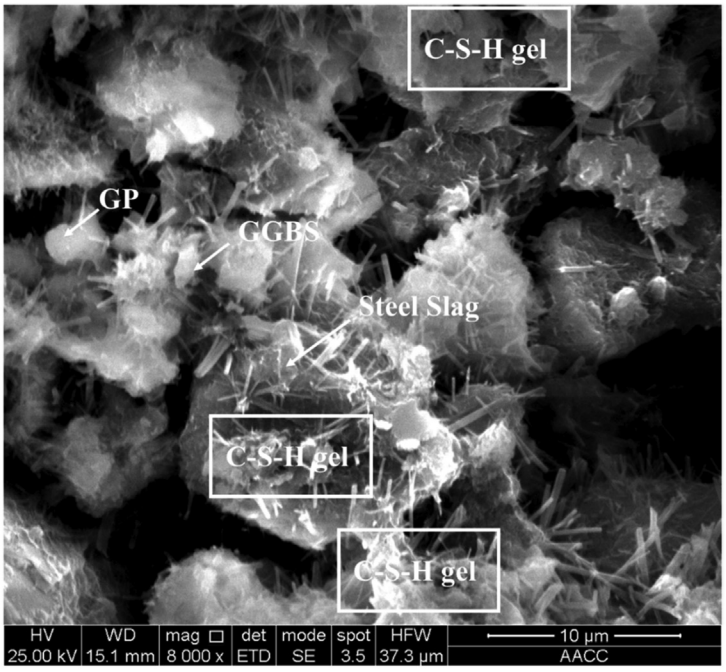

(b)

Fig. 7. SEM images of ECCC samples: (a) optimum design mixture; and (b) poor design mixture.

$$C_i = a_i \frac{\mathrm{std}(x_i)}{\mathrm{std}(y)} \tag{3}$$

where

$$y = ax + b = a_1x_1 + a_2x_2 + a_3x_3 + b \tag{4}$$

where $\times$ is the variable; y symbols the result; a and b are regression coefficients. The MATLAB software was used along with a sensitive analysis program to process the dataset collected from the experiments conducted as part of this study. The inputs were SS content, GP content, and GGBS content; whereas, the outputs were electrical resistivity, compressive strength, and flexural strength. The results of the sensitivity analysis are presented in Table 5.

For the mechanical performance, GP has the highest importance (i.e., impact on the mechanical performance) while SS has the lowest importance, which is consistent with the experimental results. For the electrical performance, GP has the highest importance (i.e., impact on the electrical performance) followed by SS then GGBS. After comprehensive consideration, GGBS is not recommended as a conductive material among the three tested materials. The results show that according to the different demands of conductive concrete, adding or replacing various components could reach the desired design. Moreover, the results also demonstrates the potential in long-term mechanical capacity improvement. Correlations between short-term (<28 days) and long-term (greater than28 days) strength of concrete were well concluded in literatures [64,65]. Additionally, the artificial intelligence includimg beetle antennae search (BAS), random forest (RF) and evolved support vector regression (ESVR) demonstrate outstanding performance in predicting the long-term strength development of cementitious material behavior [66–69].

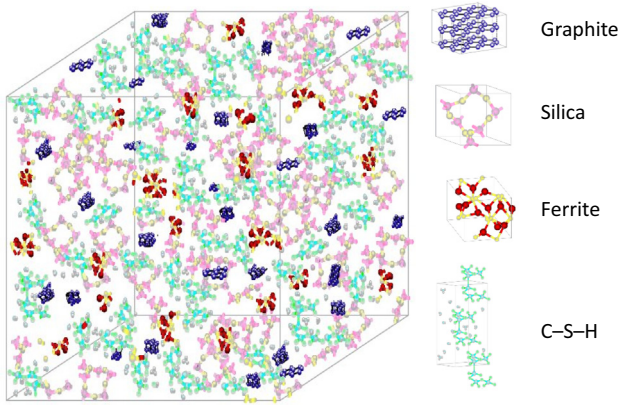

Fig. 8. Schematic diagram of conductive concrete mechanism.

Table 5
The variables sensitivity of conductive concrete.

Importance score	Compressive strength	Flexural strength	Electrical Resistivity
SS	−0.13	−0.06	−0.48
GGBS	−0.44	−0.59	−0.18
GP	−0.56	−0.73	−0.79
Rank	Compressive strength	Flexural strength	Electrical Resistivity
SS	3	3	2
GGBS	2	2	3
GP	1	1	1

4. Conclusions

In this study, a series of experiments were conducted to determine the mechanical and electrical properties of ECCCs treated with various conductive fillers including SS, GP, and GGBS. The following conclusions could be drawn from this study:

- Compared to the ordinary concrete (with no conductive fillers), the incorporation of GP into ECCCs enhances the electrical conductivity of the concrete. However, it can have an adverse effect on the mechanical behavior if its content exceeds 4%. As a result, a 4% GP ratio is recommended to achieve ECCCs with satisfactory mechanical and electrical properties.
- The incorporation of slag (SS and GGBS) into ECCCs was found to slightly enhance their mechanical performance when added with a substitution ratio up to 20%. Slag (SS and GGBS) was also found to enhance the electrical conductivity of ECCCs. SS was found to outperform GGBS in enhancing the mechanical performance and electrical performance of ECCCs during the hydration period.
- An optimized design mixture was determined to consist of 25% SS, 15% GGBS, and 4% GP. Such design was found to render compressive strength of 41.5 MPa, flexural strength of 3.5 MPa, and electrical resistivity of 1054 Ω·cm, which represent balanced characteristics compared to ordinary concrete design counterpart.
- The microstructure investigation of ECCC samples revealed that the distribution of conductive fillers and the C–S–H gel affects the mechanical and electrical performance significantly.
- The sensitivity analysis concluded a significance rank of GP followed by SS then GGBS for electrical performance, and GP followed by GGBS then SS for mechanical performance. GP reduces the resistivity of ECCCs (i.e. improves the conductivity) more than other fillers. GGBS is not recommended as conductive material after considering the effect and significance.

CRediT authorship contribution statement

Junbo Sun: Project administration, Supervision, Methodology, Conceptualization, Formal analysis. **Sen Lin:** Funding acquisition, Methodology, Data curation. **Genbao Zhang:** Funding acquisition, Conceptualization, Data curation, Visualization, Writing - original draft. **Yuantian Sun:** Methodology, Data curation. **Junfei Zhang:** Methodology, Data curation. **Changfu Chen:** Conceptualization, Data curation, Visualization. **Amr M. Morsy:** Writing - review & editing. **Xiangyu Wang:** Project administration, Supervision, Investigation.

Declaration of Competing Interest

The authors declare that they have no known competing financial interests or personal relationships that could have appeared to influence the work reported in this paper.

Acknowledgements

The authors gratefully acknowledge the financial support provided by the National Natural Science Foundation of China (grant numbers 11802082, 51908201), the Natural Science Foundation of Hunan Province (grant numbers 2020JJ5027, 2020JJ5024), and the State Key Laboratory of Advanced Design and Manufacturing for Vehicle Body (grant number 51965009).

References

[1] J. Sun et al., Properties of a double-layer EMW-absorbing structure containing a graded nano-sized absorbent combing extruded and sprayed 3D printing, Constr. Build. Mater. 261 (2020) 120031.
[2] J. Sun et al., Electromagnetic wave absorbing performance of 3D printed wave-shape copper solid cementitious element, Cem. Concr. Compos. (2020) 103789.
[3] G. Ma et al., Review on electromagnetic wave absorbing capacity improvement of cementitious material, Constr. Build. Mater. 262 (2020) 120907.
[4] Z. Wei et al., High-temperature persistent luminescence and visual dual-emitting optical temperature sensing in self-activated CaNb2O6: Tb3+ phosphor, J. Am. Ceram. Soc. (2020), https://doi.org/10.1111/jace.17579.
[5] C. Zhang, H. Wang, Swing vibration control of suspended structures using the active rotary inertia driver system: Theoretical modeling and experimental verification, Struct. Contr. Health Monit. 27 (6) (2020), https://doi.org/10.1002/stc.2543 e2543.
[6] C. Li et al., Experimental investigation and error analysis of high precision FBG displacement sensor for structural health monitoring, Int. J. Struct. Stab. Dyn. (2020) 2040011, https://doi.org/10.1142/S0219455420400118.
[7] Gao N., et al., Hybrid composite meta-porous structure for improving and broadening sound absorption, Mechanical Systems and Signal Processing 154 107504. https://doi.org/10.1016/j.ymssp.2020.107504.
[8] Y. Song et al., Traffic volume prediction with segment-based regression kriging and its implementation in assessing the impact of heavy vehicles, IEEE Trans. Intell. Transp. Syst. 20 (1) (2018) 232–243.
[9] X. Zuo et al., The modeling of the electric heating and cooling system of the integrated energy system in the coastal area, J. Coastal Res. 103 (SI) (2020) 1022–1029, https://doi.org/10.2112/SI103-213.1.
[10] C. Yang, F. Gao, M. Dong, Energy efficiency modeling of integrated energy system in coastal areas, J. Coastal Res. 103 (SI) (2020) 995–1001, https://doi.org/10.2112/SI103-207.1.
[11] C. Cai et al., Selective laser melting of near-α titanium alloy Ti-6Al-2Zr-1Mo-1V: Parameter optimization, heat treatment and mechanical performance, J. Mater. Sci. Technol. (2020), https://doi.org/10.1016/j.jmst.2020.05.004.
[12] H. Yan et al., Reversible Na+ insertion/extraction in conductive polypyrrole-decorated NaTi2 (PO4) 3 nanocomposite with outstanding electrochemical property, Appl. Surf. Sci. 530 (2020), https://doi.org/10.1016/j.apsusc.2020.147295 147295.
[13] J. Zheng, C. Zhang, A. Li, Experimental investigation on the mechanical properties of curved metallic plate dampers, Applied Sciences 10 (1) (2020) 269, https://doi.org/10.3390/app10010269.
[14] J. Zhang et al., A metaheuristic-optimized multi-output model for predicting multiple properties of pervious concrete, Constr. Build. Mater. 249 (2020) 118803.
[15] C. Cai et al., Comparative study on 3D printing of polyamide 12 by selective laser sintering and multi jet fusion, J. Mater. Process. Technol. 288 (2020), https://doi.org/10.1016/j.jmatprotec.2020.116882 116882.
[16] D.G. Meehan, S. Wang, D. Chung, Electrical-resistance-based sensing of impact damage in carbon fiber reinforced cement-based materials, J. Intell. Mater. Syst. Struct. 21 (1) (2010) 83–105.
[17] P. Wu, J. Wang, X. Wang, A critical review of the use of 3-D printing in the construction industry, Autom. Constr. 68 (2016) 21–31.
[18] X. Qu et al., Jointly dampening traffic oscillations and improving energy consumption with electric, connected and automated vehicles: A reinforcement learning based approach, Appl. Energy 257 (2020) 114030.
[19] B. Mou, Y. Bai, Experimental investigation on shear behavior of steel beam-to-CFST column connections with irregular panel zone, Eng. Struct. 168 (2018) 487–504, https://doi.org/10.1016/j.engstruct.2018.04.029.
[20] L. Wang et al., Practical algorithm for stochastic optimal control problem about microbial fermentation in batch culture, Optimization Letters 13 (3) (2019) 527–541.
[21] A.S. El-Dieb et al., Multifunctional electrically conductive concrete using different fillers, J. Build. Eng. 15 (2018) 61–69.
[22] B. Han, S. Ding, X. Yu, Intrinsic self-sensing concrete and structures: A review, Measurement 59 (2015) 110–128.
[23] P. Wang et al., A superhydrophobic/electrothermal synergistically anti-icing strategy based on graphene composite, Compos. Sci. Technol. 198 (2020), https://doi.org/10.1016/j.compscitech.2020.108307 108307.
[24] P. Wang et al., Superhydrophobic flexible supercapacitors formed by integrating hydrogel with functional carbon nanomaterials. Chinese Journal of Chemistry cjoc.202000543. Doi: https://doi.org/10.1002/cjoc.202000543.
[25] Z. Huang et al., Parameter analysis of damaged region for laminates with matrix defects. Journal of Sandwich Structures & Materials: p. 1099636219842290. 2019, Doi: https://doi.org/10.1177/1099636219842290.
[26] S. Sun et al., Multi-layer graphene-engineered cementitious composites with multifunctionality/intelligence, Compos. B Eng. 129 (2017) 221–232.
[27] A.P. Singh et al., Graphene oxide/ferrofluid/cement composites for electromagnetic interference shielding application, Nanotechnology 22 (46) (2011) 465701.
[28] J. Chen et al., Graphene oxide-deposited carbon fiber/cement composites for electromagnetic interference shielding application, Constr. Build. Mater. 84 (2015) 66–72.
[29] M.S. Konsta-Gdoutos, C.A. Aza, Self sensing carbon nanotube (CNT) and nanofiber (CNF) cementitious composites for real time damage assessment in smart structures, Cem. Concr. Compos. 53 (2014) 162–169.
[30] C. Cai et al., Hot isostatic pressing of a near α-Ti alloy: Temperature optimization, microstructural evolution and mechanical performance evaluation, Mater. Sci. Eng., A (2020), https://doi.org/10.1016/j.msea.2020.140426 140426.
[31] S. Chen, M. Hassanzadeh-Aghdam, R. Ansari, An analytical model for elastic modulus calculation of SiC whisker-reinforced hybrid metal matrix nanocomposite containing SiC nanoparticles, J. Alloy. Compd. 767 (2018) 632–641, https://doi.org/10.1016/j.jallcom.2018.07.102.
[32] H. Yu et al., The NOx degradation performance of Nano-TiO2 coating for asphalt pavement, Nanomaterials 10 (5) (2020) 897, https://doi.org/10.3390/nano10050897.
[33] H. Zhao et al., Catalytic reforming of volatiles from co-pyrolysis of lignite blended with corn straw over three different structures of iron ores, J. Anal. Appl. Pyrol. 144 (2019), https://doi.org/10.1016/j.jaap.2019.104714 104714.
[34] H. Yu et al., Evaluation of phosphorus slag (PS) content and particle size on the performance modification effect of asphalt, Constr. Build. Mater. 256 (2020), https://doi.org/10.1016/j.conbuildmat.2020.119334 119334.
[35] H. Li et al., Hamiltonian analysis of a hydro-energy generation system in the transient of sudden load increasing, Appl. Energy 185 (2017) 244–253.
[36] J. Liu, Y. Yi, X. Wang, Exploring factors influencing construction waste reduction: A structural equation modeling approach, J. Cleaner Prod. 276 (2020), https://doi.org/10.1016/j.jclepro.2020.123185 123185.
[37] Y. Ju, T. Shen, D. Wang, Bonding behavior between reactive powder concrete and normal strength concrete, Constr. Build. Mater. 242 (2020), https://doi.org/10.1016/j.conbuildmat.2020.118024 118024.
[38] M. Abedini et al., Large deflection behavior effect in reinforced concrete columns exposed to extreme dynamic loads, Front. Struct. Civ. Eng. 14 (2) (2020) 532–553, https://doi.org/10.1007/s11709-020-0604-9.
[39] F. Aslani et al., Fiber-reinforced lightweight self-compacting concrete incorporating scoria aggregates at elevated temperatures, Structural Concrete 20 (3) (2019) 1022–1035.
[40] S. Ahmari, K. Parameswaran, L. Zhang, Alkali activation of copper mine tailings and low-calcium flash-furnace copper smelter slag, J. Mater. Civ. Eng. 27 (6) (2014) 04014193.
[41] A. Nazer et al., Use of ancient copper slags in Portland cement and alkali activated cement matrices, J. Environ. Manage. 167 (2016) 115.
[42] G. Gelardi, R. Flatt, Working mechanisms of water reducers and superplasticizers, in Science and Technology of Concrete Admixtures. 2016, Elsevier. p. 257–278.
[43] C. Zhang, G. Gholipour, A.A. Mousavi, State-of-the-art review on responses of RC structures subjected to lateral impact loads, Arch. Comput. Methods Eng. (2020) 1–31, https://doi.org/10.1007/s11831-020-09467-5.
[44] R. Yao et al., Preparation and characterization of novel glass–ceramic tile with microwave absorption properties from iron ore tailings, J. Magn. Magn. Mater. 378 (2015) 367–375.
[45] YB/T 4177-2008, Determination of chemical composition in slag by X-ray fluorescence spectrometry, 2008, p. 39-40.
[46] L. Jia et al., Structure design of MoS 2@ Mo 2 C on nitrogen-doped carbon for enhanced alkaline hydrogen evolution reaction, J. Mater. Sci. 55 (34) (2020) 16197–16210, https://doi.org/10.1007/s10853-020-05107-2.
[47] K. Janković et al., The influence of nano-silica and barite aggregate on properties of ultra high performance concrete, Constr. Build. Mater. 126 (2016) 147–156.
[48] Ono, A., et al., Ultrarapid hardening cement composition and dispersant for ultrarapid hardening cement composition. 2011, U.S. Patent 8,076,396, issued December 13, 2011.
[49] AS1141.51, Methods for sampling and testing aggregates, Method 51: Unconfined compressive strength of compacted materials. AS-1141.51, 1996.
[50] F.J. Baeza et al., Influence of recycled slag aggregates on the conductivity and strain sensing capacity of carbon fiber reinforced cement mortars, Constr. Build. Mater. 184 (2018) 311–319.
[51] C. Zhang, M. Abedini, J. Mehrmashhadi, Development of pressure-impulse models and residual capacity assessment of RC columns using high fidelity Arbitrary Lagrangian-Eulerian simulation, Eng. Struct. 224 (2020), https://doi.org/10.1016/j.engstruct.2020.111219 111219.
[52] AS1012.14, Methods of testing concrete: method 14: method for securing and testing cores from hardened concrete for compressive strength. Materials Tests, 1991.
[53] AS1012.9, Methods of testing concrete, compressive strength tests - concrete, mortar and grout specimens. 2014, Author Sydney.
[54] H. Huang et al., Experimental investigation on rehabilitation of corroded RC columns with BSP and HPFL under combined loadings, J. Struct. Eng. 146 (8) (2020) 04020157, https://doi.org/10.1061/%28ASCE%29ST.1943-541X.0002725.
[55] L. Sun et al., Effect of axial compression ratio on seismic behavior of GFRP reinforced concrete columns, Int. J. Struct. Stab. Dyn. (2020) 2040004, https://doi.org/10.1142/S0219455420400040.
[56] H. Sun et al., High-resolution anisotropic prestack Kirchhoff dynamic focused beam migration, IEEE Sens. J. (2019), https://doi.org/10.1109/JSEN.2019.2933200.
[57] B. Mou et al., Flexural behavior of beam to column joints with or without an overlying concrete slab, Eng. Struct. 199 (2019), https://doi.org/10.1016/j.engstruct.2019.109616 109616.
[58] B. Mou et al., Shear behavior of panel zones in steel beam-to-column connections with unequal depth of outer annular stiffener, J. Struct. Eng. 145 (2) (2019) 04018247, https://doi.org/10.1061/(ASCE)ST.1943-541X.0002256.

[59] M. Abedini, C. Zhang, Blast performance of concrete columns retrofitted with FRP using segment pressure technique, Compos. Struct. (2020) 113473.
[60] G. Gholipour, C. Zhang, A.A. Mousavi, Numerical analysis of axially loaded RC columns subjected to the combination of impact and blast loads, Eng. Struct. 219 (2020), https://doi.org/10.1016/j.engstruct.2020.110924 110924.
[61] Zhang C., Mousavi A.A., Blast loads induced responses of RC structural members: State-of-the-art review, Composites Part B: Engineering 2020 108066. Doi. https://doi.org/10.1016/j.compositesb.2020.108066.
[62] Y. Zhang et al., Emergence of skyrmionium in a two-dimensional CrGe (Se, Te) 3 Janus monolayer, Physical Review B 102 (24) (2020), https://doi.org/10.1103/PhysRevB.102.241107 241107.
[63] M. Abedini et al. Comparison of ALE, LBE and pressure time history methods to evaluate extreme loading effects in RC column. in Structures. 2020. Elsevier. Doi: https://doi.org/10.1016/j.istruc.2020.08.084.
[64] M.S. Mamlouk, J.P. Zaniewski, Materials for civil and construction engineers, Pearson Prentice Hall Upper Saddle River, NJ, 2006.
[65] Y. Sun et al., Development of an ensemble intelligent model for assessing the strength of cemented paste backfill, Advances in Civil Engineering (2020), https://doi.org/10.1155/2020/1643529. Article ID 1643529.
[66] J. Sun et al., Prediction of permeability and unconfined compressive strength of pervious concrete using evolved support vector regression, Constr. Build. Mater. 207 (2019) 440–449.
[67] Y. Sun et al., Optimized neural network using beetle antennae search for predicting the unconfined compressive strength of jet grouting coalcretes, Int. J. Numer. Anal. Meth. Geomech. 43 (4) (2019) 801–813.
[68] Y. Sun et al., Determination of Young's modulus of jet grouted coalcretes using an intelligent model, Eng. Geol. 252 (2019) 43–53.
[69] J. Zhang et al., Modelling uniaxial compressive strength of lightweight self-compacting concrete using random forest regression, Constr. Build. Mater. 210 (2019) 713–719.
[70] Failure Process of Modeled Recycled Aggregate Concrete under Uniaxial Compression 13 (19) (2020) 4329, doi:https://doi.org/10.3390/ma13194329.